A laboratory model for the Parker spiral and magnetized stellar winds

Ethan E. Peterson [1]*, Douglass A. Endrizzi [1], Matthew Beidler[2,3], Kyle J. Bunkers[1], Michael Clark[1], Jan Egedal[1], Ken Flanagan [1], Karsten J. McCollam[1], Jason Milhone [1], Joseph Olson [1], Carl R. Sovinec [2], Roger Waleffe [1], John Wallace[1] and Cary B. Forest[1]

Many rotating stars have magnetic fields that interact with the winds they produce. The Sun is no exception. The interaction between the Sun's magnetic field and the solar wind gives rise to the heliospheric magnetic field—a spiralling magnetic structure, known as the Parker spiral, which pervades the Solar System. This magnetic field is critical for governing plasma processes that source the solar wind. Here, we report the creation of a laboratory model of the Parker spiral system based on a rapidly rotating plasma magnetosphere and the measurement of its global structure and dynamic behaviour. This laboratory system exhibits regions where the plasma flows evolve in a similar manner to many magnetized stellar winds. We observe the advection of the magnetic field into an Archimedean spiral and the ejection of quasi-periodic plasma blobs into the stellar outflow, which mimics the observed plasmoids that fuel the slow solar wind. This process involves magnetic reconnection and can be modelled numerically by the inclusion of two-fluid effects in the simulation. The Parker spiral system mimicked in the laboratory can be used for studying solar wind dynamics in a complementary fashion to conventional space missions such as NASA's Parker Solar Probe mission.

In 1958, Eugene Parker first predicted the existence of the supersonic solar wind[1], which was subsequently verified by early spacecraft missions[2,3]. He also theorized how this solar wind interacts with the dynamo-generated magnetic field of the Sun—carrying the magnetic field lines away from the star, while their footpoints are frozen into the corona and twisted into an Archimedean spiral by stellar rotation. This magnetic topology is now known as the Parker spiral and is the largest magnetic structure in the heliosphere. The transition between the magnetic field co-rotating with a star and the field advected by the wind is thought to occur near the so-called Alfvén surface, where inertial forces in the wind can stretch and bend the magnetic field. According to the governing equations of magnetohydrodynamics (MHD), this transition in a magnetic field like that of the Sun is singular in nature and therefore suspected to be highly dynamic[4,5]. However, this region has rarely been observed in situ by spacecraft and is presently the primary focus of the Parker Solar Probe mission[6,7]. Here we show, in a synergistic approach to studying solar wind dynamics, that the large-scale magnetic topology of the Parker spiral can also be created and studied in the laboratory. By generating a rotating magnetosphere with Alfvénic flows, magnetic field lines are advected into an Archimedean spiral, giving rise to a dynamic current sheet that undergoes magnetic reconnection and plasmoid ejection. These plasmoids are born near the Alfvén surface, at the tip of the helmet streamer, and carry blobs of plasma outwards at super-Alfvénic speeds, mimicking the dynamics of unstable coronal helmet streamers, which are thought to fuel a significant portion of the slow solar wind[8–10].

As the solar wind evolves from the lower corona to 1 au, the governing dynamics change dramatically as the plasma is accelerated outward and the magnetic field of the Sun decreases. The solar wind experiences three primary dynamical interfaces—regions where the dominant plasma forces change in nature. These three interfaces are the transonic, trans-Alfvénic and trans-β zones[1,11,12]. They characterize where the solar wind speed becomes supersonic, where it becomes super-Alfvénic (inertial forces dominate magnetic forces, that is $V_{Alfven} = B/\sqrt{\mu_0 m_i n} < V_{sw}$), and where the plasma pressure overcomes the magnetic pressure (that is, $\beta = 2\mu_0 nT/B^2 > 1$), respectively. These transition zones depend on the magnetic field strength B, the plasma density n, the plasma temperature T, the ion mass m_i and the local solar wind speed V_{sw}. As a result, the transitions are governed by the interaction between the magnetic topology of the Sun and the plasma acceleration and heating mechanisms in the corona. This interaction results in complex, often overlapping, transition zones that vary wildly with heliographic latitude as well as heliocentric distance and give rise to the wide range of characteristics exhibited by the solar wind[13,14].

Many spacecraft missions since the early 1960s have been dedicated to observing and categorizing the composition, speed, density and magnetic field of the solar wind from various vantage points to gain insight into the origins and acceleration of the solar wind[15]. Possibly none of these missions is more famous than Ulysses, which was the first to fly over the solar poles and discovered that the 'fast' solar wind tends to come from the open field lines of coronal holes, whereas the 'slow' solar wind has its origins in the equatorial streamer belt[16]. However, the mechanisms that transport the slow solar wind plasma from closed field lines in the streamer belt to the open field lines of the Parker spiral are more ambiguous and have motivated theoretical, computational and observational work dedicated to elucidating this issue[5,17–20]. Despite the fundamental role these dynamical interfaces play in the origin and evolution of the solar wind, they have received little experimental attention. Nevertheless, a laboratory model of this system is not only possible, but provides new insight into the behaviour of dynamical interfaces

[1]Department of Physics, University of Wisconsin–Madison, Madison, WI, USA. [2]Engineering Physics Department, University of Wisconsin–Madison, Madison, WI, USA. [3]Present address: Oak Ridge National Laboratory, Oak Ridge, TN, USA. *e-mail: eepeterson3@gmail.com
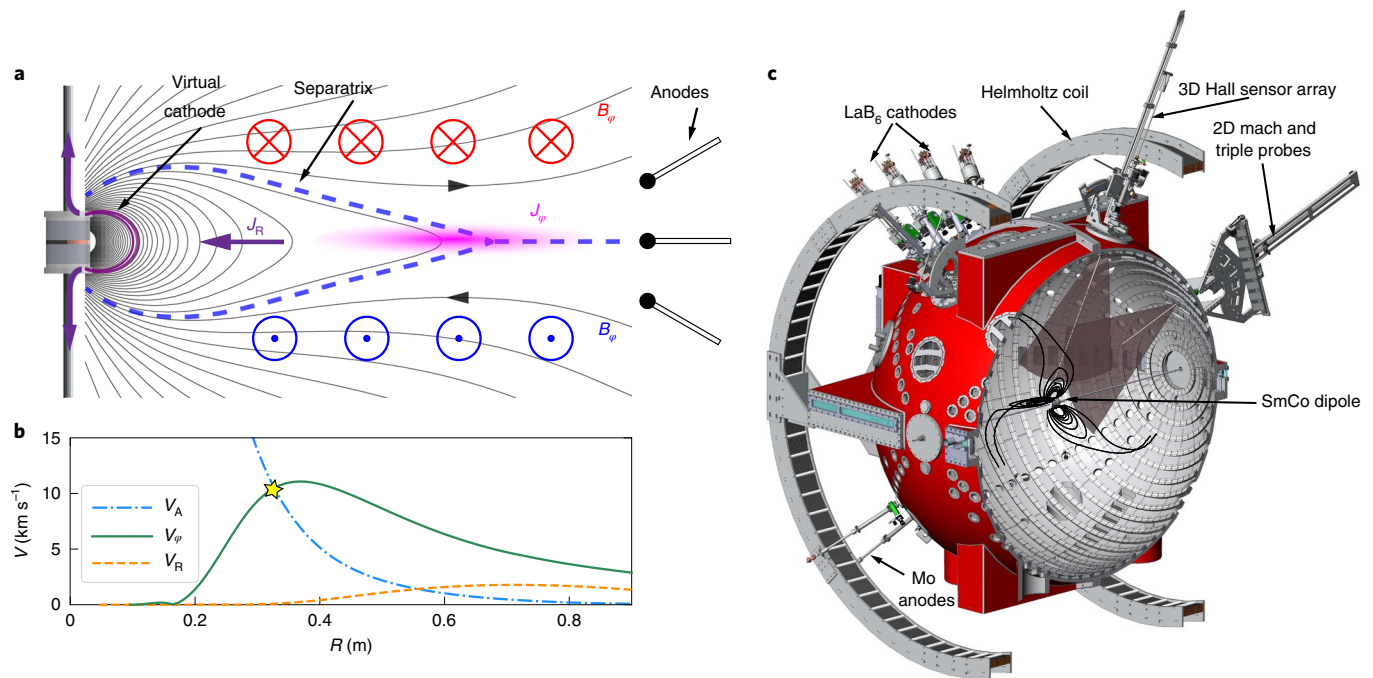
Fig. 1 | A laboratory recipe for creating a Parker spiral and stellar wind. a, Drawing current from anodes in the plasma atmosphere to a virtual cathode in the magnetosphere creates a cross field current J_R and associated torque on the plasma. **b**, This torque drives plasma rotation, shown by the toroidal velocity V_φ (green solid line). The rotation becomes super-Alfvénic at the radius denoted by the star when the rotation speed surpasses the Alfvén speed, V_A (blue dash-dotted line). This super-Alfvénic rotation launches a radial wind shown by V_R (orange dashed line). This wind then stretches the magnetic field lines outwards while they are twisted into a spiral by rapid rotation, forming the magnetic structures shown in **a**. This evolution produces a separatrix between the closed and open flux surfaces—a characteristic that is universal to many magnetized winds, and the understanding of which is vital to the study of stellar momentum transport and evolution. The experimental procedure to create the Parker spiral system is described in more detail in the Methods. **c**, Schematic of the experiment.

relevant to the evolution of stellar winds, with special attention given to the dynamics near the Alfvén and $\beta = 1$ surfaces.

In this Article, we report the creation of a laboratory model of the Parker spiral system and the measurement of its global structure and dynamic behaviour. This system is realized by producing a rotating plasma magnetosphere whose magnetic topology evolves from a closed magnetosphere into an Archimedean spiral. We show that this system develops interface regions where $V \approx V_{\text{Alfvén}}$ and $\beta \approx 1$, which become highly dynamic and result in processes that transport plasma from closed dipolar flux surfaces out to the open field lines of the Parker spiral. The experiments are compared to two-dimensional (2D) extended magnetohydrodynamic (MHD) simulations performed with the NIMROD code[21], which convincingly show that two-fluid (Hall) effects are essential for understanding the current sheet and flows that develop. These experiments were carried out in the Big Red Ball (BRB) device at the Wisconsin Plasma Physics Laboratory (WiPPL)[22]. The BRB, shown in Fig. 1c, is a versatile 3-m-diameter multi-dipole confinement device capable of confining high-ionization-fraction, unmagnetized plasmas, and is well suited for investigations of basic plasma systems and phenomena.

To create a rotating stellar wind in the laboratory, we use a dipole magnet similar to previous terella experiments[23,24], but embed the artificial magnetosphere in a much larger unmagnetized plasma atmosphere. We then employ electromagnetic stirring techniques[25,26] to produce rotation comparable to the Alfvén speed, as outlined in Fig. 1b and described in detail in the Methods. When the plasma rotation reaches the Alfvén speed, the centrifugal force of the wind overwhelms the magnetic confining force and the plasma can inertially break free from the magnetosphere, stretching and twisting the magnetic field into a Parker spiral (Fig. 1a,c).

The remainder of this Article presents the measurements of this laboratory Parker spiral, demonstrating three major findings: (1) the magnetic field is advected into an Archimedean spiral, (2) the associated current sheet is dynamic and produces plasmoids near the Alfvén radius, (3) these plasmoids travel outwards at super-Alfvénic speeds and can be understood through the lens of Hall-MHD. For comparison to the dynamics of the solar wind, Table 1 outlines some dimensionless parameters relating this experiment in the BRB to the solar wind. Although this laboratory system cannot reflect the scale of the heliosphere, has no appreciable gravitational effects, has a constrained return current path and does not produce supersonic flows, it nevertheless recreates the macroscopic topology of stellar magnetic fields like the Parker spiral and its interactions with Alfvénic plasma flows.

We begin, for context, by summarizing the time dynamics of a shot sequence as shown in Fig. 2. Important to note are the two distinct phases present, which are characterized by an initial, non-axisymmetric state with large broadband fluctuations (phase I) and an axisymmetric, coherent, unstable state (phase II). A snapshot of visible light captured by a fast camera during each of these two phases shows non-axisymmetric density structures that follow the spiralling magnetic field in phase I (Fig. 2e) and a more diffuse, axisymmetric density in phase II (Fig. 2f). Power spectral densities of magnetic and density fluctuations in the current sheet during these two phases confirm the presence of coherent modes arising after a period of high-amplitude broadband fluctuations (Fig. 2d). Although phase I exhibits interesting dynamics, in this study we focus on the mean field quantities and coherent modes during the axisymmetric phase II.

Mapping out the time-resolved, 2D structure of the Parker spiral is performed with linear arrays of three-axis Hall sensors, mach

	Re	Rm	L/λ_e	L/λ_i	$\Omega_{ce}\tau_e$	$\Omega_{ci}\tau_i$
BRB	35	50	0.3	30	250	0.05
Solar wind	20	10^{14}	2	2	10^8	10^6

The Reynolds number Re is comparable in both cases, implying similar hydrodynamic behaviour. Both systems exhibit magnetic Reynolds numbers $Rm \gg 1$, indicating low magnetic diffusivity as well as circumstances where magnetic diffusion dominates magnetic diffusion, namely the magnetic Prandtl number $Pm = Rm/Re > 1$. The electron and ion collisionality, given by L/λ_e and L/λ_i, respectively, expresses how many collisions a particle experiences as it transits across a system of size L, where λ_e and λ_i are the electron and ion mean free paths. One can see that electrons suffer a similar number of collisions in both systems. However, in the experiment the ions are much more collisional than in the solar wind. The magnetization of electrons and ions indicates how many gyro-orbits a particle undergoes before suffering a collision and is given by $\Omega_{ce}\tau_e$ and $\Omega_{ci}\tau_i$, where Ω_{ce} and Ω_{ci} are the electron and ion cyclotron frequencies, respectively, and τ_e and τ_i are characteristic electron and ion collision times. Therefore, the electrons are highly magnetized in both systems, whereas the ions are only magnetized in the solar wind. The estimates of parameters for the BRB were made using a system size of $L = 30$ cm. Estimates for the solar wind were made from fits to spacecraft data in the ecliptic plane[27] and were taken at $5R_\odot$, using $L = 5R_\odot$. In summary, both systems demonstrate relatively collisionless, magnetized electrons with $Rm \gg 1$ and $Pm > 1$. However, the ions in the BRB are neither collisionless nor magnetized.

probes and triple probes. The resulting measurements of the magnetic field structure and comparison to simulations are provided in Fig. 3. Figure 3a shows that the contours of the poloidal magnetic flux (black lines) form an elongated magnetosphere. This figure also shows antiparallel toroidal magnetic fields above and below the current sheet (cyan dashed line), with an up–down asymmetry caused by preferential current drawn to an anode below the equator in the plasma atmosphere. The data shown in Fig. 3a are compared to MHD and Hall-MHD simulations (Fig. 3c,d). The Hall case shows closer agreement to the data as more magnetic flux is expelled from the magnetosphere (Fig. 3b), leading to higher values of β and larger magnetic curvature in the current sheet. An axisymmetric 3D rendering of field lines from data measured by magnetic probes reveals the Parker spiral topology with antiparallel toroidal fields above and below the closed field region (Fig. 3e).

In addition to the magnetic structures, the plasma flows were measured and similarly compared to the aforementioned NIMROD simulations in Fig. 4. The results confirm that the toroidal flow in the experiment approaches the Alfvén speed in the current sheet with a peak at Alfvén radius $R_{\text{Alfvén}} = 30$ cm, shown in Fig. 4b. From Fig. 4b it is also clear that the rotation becomes super-Alfvénic in the MHD simulation (Fig. 4c), whereas rotation in the Hall-MHD model (Fig. 4d) is limited to $M_{\text{Alfvén}} \approx 1$ and is consistent with the experiment. The mean radial flow along the current sheet in the experiment was measured to be indistinguishable from zero and is once again in closer agreement with the Hall-MHD model, which produces a weakly accreting magnetosphere rather than a radial wind as in the MHD simulation. The experiment succeeded in creating a rapidly rotating magnetosphere with peaked rotation rates comparable to the local Alfvén speed. It is important to note that the peak in the $M_{\text{Alfvén}}$ profile occurs around $R = 30$ cm, which corresponds to the location where magnetic reconnection and plasmoid formation take place.

The 2D reconstruction of the magnetic fluctuations was performed using amplitude and phase correlations with a fixed reference magnetic probe displaced 100° toroidally from the swept probe. The correlations confirmed the fluctuations to be axisymmetric, corroborating the video evidence of axisymmetric 'strobing' of visible light emission present near the end of Supplementary Video 1. This reconstruction revealed a periodic reconnection process occuring near the Alfvén radius, which releases plasmoids into the current sheet at a frequency of 20 kHz. The resulting time dynamics of the plasmoid ejection process are shown in Supplementary Video 2,
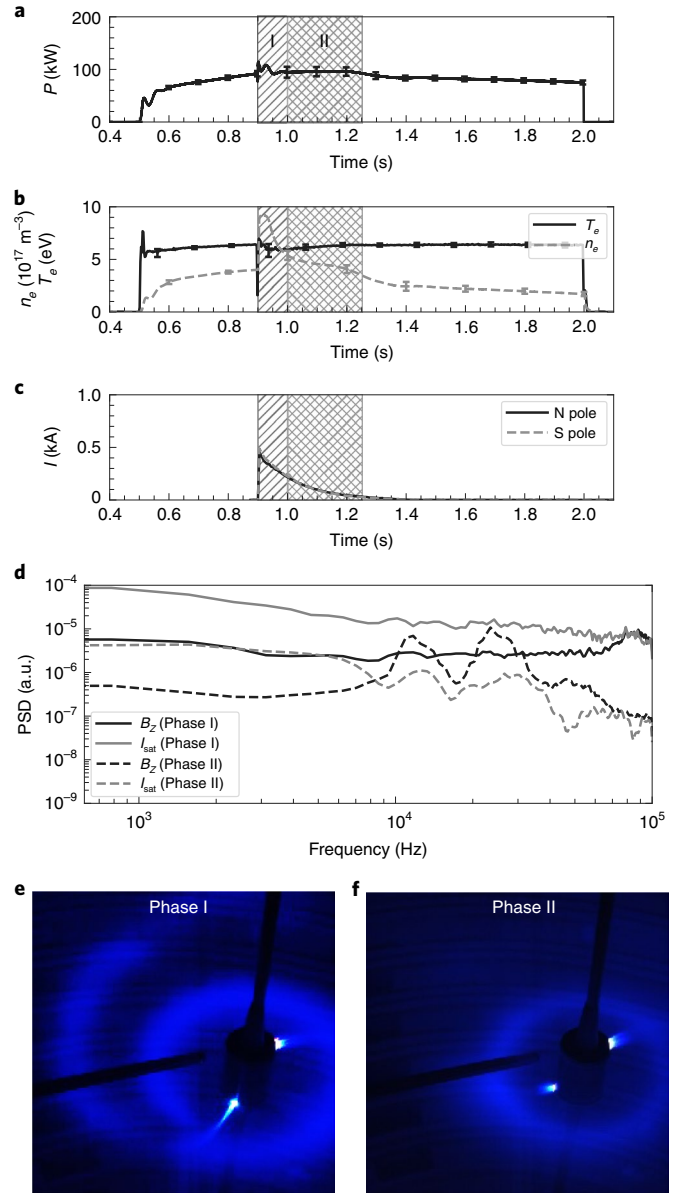

Fig. 2 | Magnetospheric evolution exhibits two distinct phases. An initial period of large-amplitude, non-axisymmetric, broadband fluctuations is followed by a quiescent, axisymmetric, coherent instability. **a**–**c**, Time dynamics of LaB_6 cathode input power (P) (**a**), electron temperature (T_e) and density (n_e) (**b**) and polar cathode current injection (I) at both the north (N) and south (S) poles of the dipole magnet (**c**) show the duration of these two phases denoted by the different hatched regions. **d**, Power spectral densities (PSDs) for magnetic field B_Z and density fluctuations computed from ion saturation current I_{sat} measurements, with higher levels during phase I and coherent modes arising later in phase II. a.u., arbitrary units. **e**,**f**, Visible light emission imaged with a Phantom camera is shown for non-axisymmetric (**e**, phase I) and axisymmetric (**f**, phase II) periods. Error bars indicate s.d. for the full ensemble of shots as a measure of shot to shot reproducibility.

which shows that plasmoids are ejected into the current sheet with higher densities than the ambient plasma by ~10%. Interestingly, when compared to simulations, the Hall-MHD model produced plasmoids of remarkably similar frequency to the experiment at 15 kHz (Supplementary Video 3), whereas the MHD case produced none. Tracking the propagation speed of plasmoids in both the
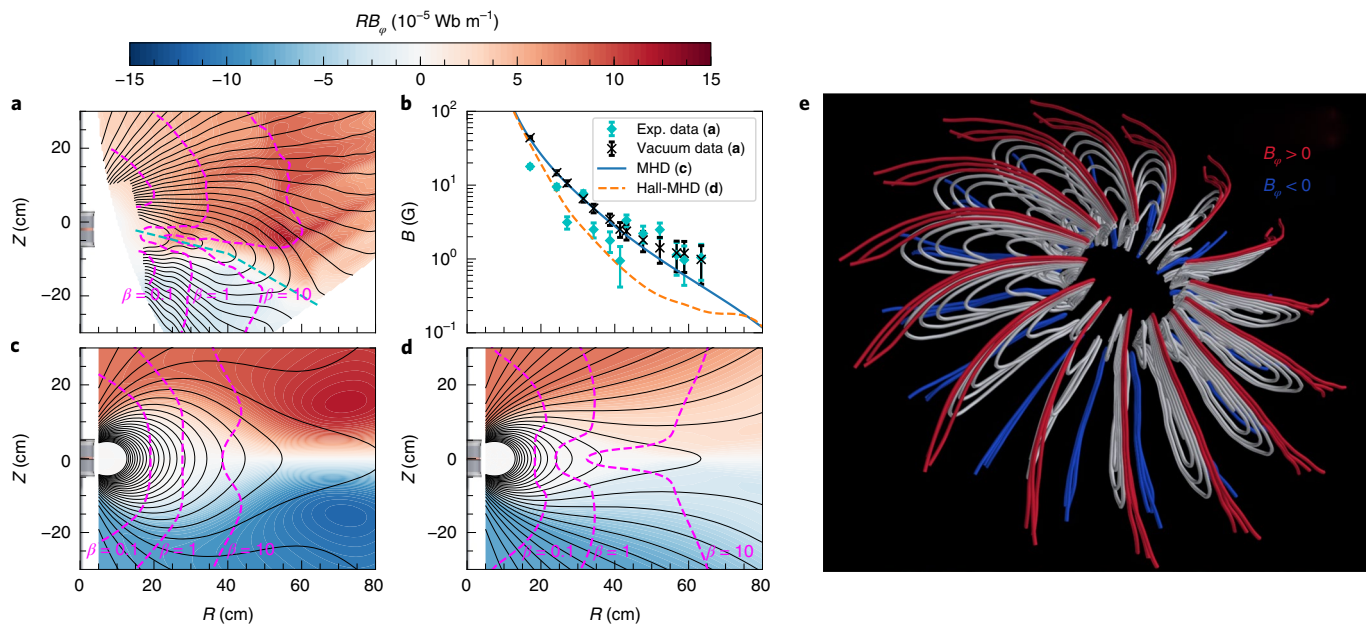
RB_φ (10^{-5} Wb m^{-1})

Fig. 3 | Measured and simulated 3D magnetic fields result in a Parker spiral. Black contour lines show the in-plane (poloidal) magnetic flux, whereas the colour contours represent the out-of-plane (toroidal) magnetic field multiplied by cylindrical radius R. **a,c,d**, Magenta contours show the $\beta = 0.1$, 1, 10 surfaces and demonstrate that the experiment and Hall-MHD simulation expel more flux from the helmet streamer than in the MHD case. **b**, This is corroborated by radial profiles of the poloidal field strength before the plasma, given by the vacuum data, and during the experiment and simulations. These radial profiles are taken along the current sheet denoted by the cyan dashed line in **a** and $Z = 0$ in **c** and **d**. Error bars in **b** represent s.d. error estimates in the measured magnetic field along the current sheet. **e**, Axisymmetric rendering of the Parker spiral obtained by integrating the field line equations using magnetic probe measurements at one toroidal angle. This 3D structure is then repeated an arbitrary number of times to give the reader a sense of the measured Parker spiral's axisymmetric nature. The colour scheme applied to this rendering is red for open field lines with $B_\varphi > 0$, blue for open field lines with $B_\varphi < 0$ and white for the closed field lines.
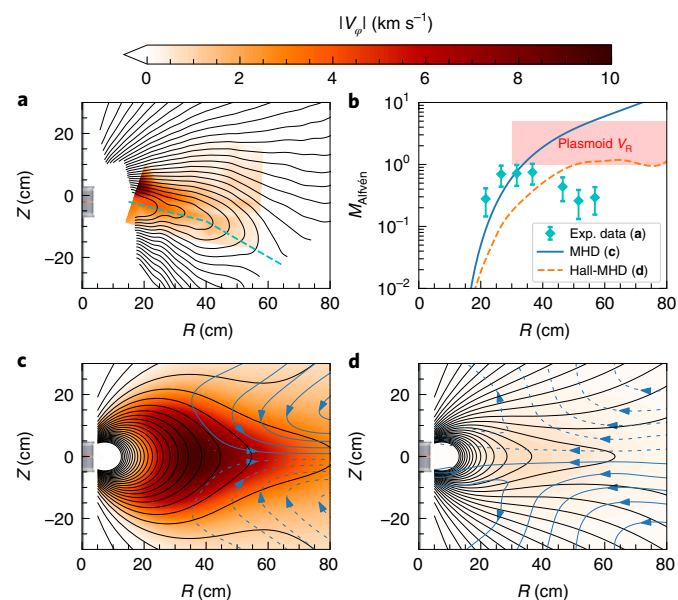
$|V_\varphi|$ (km s^{-1})

Fig. 4 | Measured rotation approaches the Alfvén speed along the current sheet. a,c,d, Measurements of toroidal rotation speeds V_φ are shown in **a** and compared to MHD (**c**) and Hall-MHD simulations (**d**). Blue contour lines with arrows in **c** and **d** depict streamlines of the poloidal plasma flow in the MHD and Hall-MHD simulations, respectively. **b**, The Hall-MHD case shows much slower rotation, but also expels more magnetic flux such that the flow is still marginally Alfvénic (orange dashed line). However, the radial flow is small and directed inward in the Hall-MHD simulation, forming a weakly accreting magnetosphere. The cyan data points represent profile measurements of toroidal ion flow along the current sheet (cyan dashed line in **a**) normalized to the local Alfvén speed. This shows a peak in the Alfvén mach number profile of $M_{Alfvén} = 0.8 \pm 0.2$ (error bars indicate s.d. error estimates for $M_{Alfvén}$) at $R = 30$ cm. These data are compared to the toroidal velocity profiles along $Z = 0$ cm for the MHD and Hall-MHD models (likewise normalized to the local Alfvén speed). The red shaded region represents the range of plasmoid radial flow speeds as measured in the experiment.
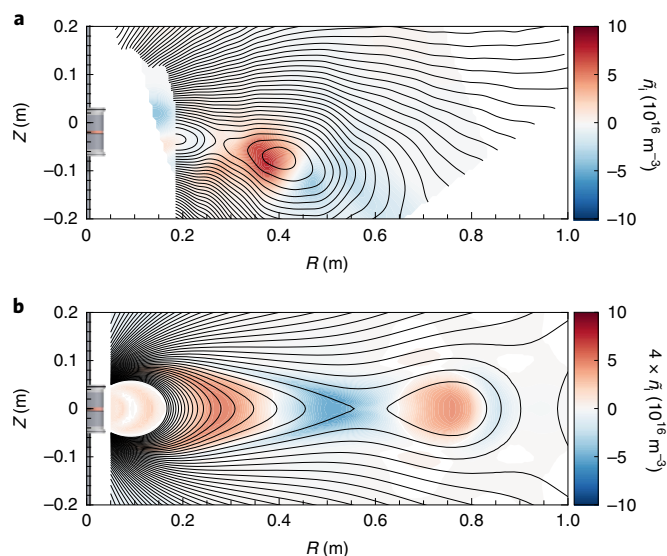
Fig. 5 | Plasmoid ejection occurs in both the experiment and Hall-MHD simulation. Pressure enhancement in the interior closed flux region causes field lines inside the 'Y'-point to balloon outward—stretching and eventually reconnecting to eject plasmoids. Videos of the experimental plasmoids and Hall-MHD simulation plasmoids are provided in Supplementary Videos 2 and 3, respectively. These videos show the experimental plasmoids to have velocities of 5–10 km s^{-1} as they travel from the Alfvén surface at $R = 30$ cm to $R = 60$ cm. Over this distance, the local Alfvén speed drops from 4 km s^{-1} to 2 km s^{-1}, giving these plasmoids an Alfvén mach number range of 1–5. The Hall-MHD simulation plasmoid velocities agree well with the experimental measurements at 6–8 km s^{-1}.

experiment and Hall-MHD simulation shows they travel outwards at super-Alfvénic speeds as described in Fig. 5 and Supplementary Videos 2 and 3. The plasmoid evolution involves a periodic build up of plasma pressure inside the Alfvén surface causing field line stretching, reconnection and plasmoid ejection. This is attributed in part to the accretion present in the Hall-MHD model as well as ionization along the virtual cathode fluxtube in the experiment, which is not modelled in the simulations. In the MHD model, the presence of the radial wind does not allow the pressure to build up in this region, and as a result, produces no plasmoids.

This plasmoid formation process is consistent with pressure and centrifugally driven ballooning modes observed in the Earth's magnetotail[28] and the Jovian magnetosphere[29]. Pressure and centrifugal forces stretch the dipole field lines until they reconnect, forming plasmoids in the current sheet. In the solar corona, a similar process is plausible at the tips of the helmet streamers, where a trans-β region can be expected as the field decreases approaching the magnetic null at the 'Y'-point. One would expect these processes to transport plasma from closed to open flux surfaces near the trans-β zone of the solar magnetic equator[30,31]. It is important to note that the ion skin depth in our plasma atmosphere is ~70 cm. This means the plasmoid and current sheet widths are on the order of ~10d_e, where d_e is the electron skin depth and represents the length scale at which electron motions are no longer frozen with the magnetic field. Therefore, just as reconnection involves physics at the electron scale and is the focus of the Magnetospheric Multiscale mission (MMS)[32], this related problem of plasma detachment from the solar corona at helmet streamer tips may also be governed by electron-scale physics. In fact, previous work has shown two-fluid effects to be important in the ejection of plasmoids from coronal helmet streamers and in understanding the coupling of electron and ion fluids at the boundary of closed and open magnetic flux[33].

In summary, we have created a laboratory model of the Parker spiral and showed that it exhibits trans-β and trans-Alfvénic zones, much like many magnetized stellar winds. By creating a rapidly rotating plasma magnetosphere we stretch and twist the magnetic field into an Archimedean spiral, successfully mimicking the global magnetic topology of the heliosphere. Doing so produces a dynamic interface region between closed field lines of the magnetosphere and the open field lines of the Parker spiral, forming a current sheet and a 'Y'-point.

At this interface between closed and open magnetic fields, the toroidal current and poloidal magnetic field produce an inward directed electric field via the Hall effect. This electric field acts to draw ions inward while accelerating electrons outward. As the ion density builds up in the closed field region it causes the magnetic field to balloon outward into the current sheet until the field can reconnect, ejecting plasmoids with enhanced density into the out-flow. These quasi-periodic plasmoids are observed in our experiment and mimic the observed plasmoids ejected from the tips of helmet streamers that fuel the slow solar wind.

This experiment demonstrates that laboratory facilities possess abilities complementary to in situ spacecraft missions and are capable of studying a wide range of physical phenomena relevant to the origin and evolution of magnetized stellar winds.

Online content

Any methods, additional references, Nature Research reporting summaries, source data, statements of code and data availability and associated accession codes are available at https://doi.org/10.1038/s41567-019-0592-7.

References

1. Parker, E. N. Dynamics of the interplanetary gas and magnetic fields. *Astrophys. J.* **128**, 664–676 (1958).
2. Gringauz, K. I., Bezrokikh, V. V., Ozerov, V. D. & Rybchinskii, R. E. A study of the interplanetary ionized gas, high-energy electrons and corpuscular radiation from the Sun by means of the three-electrode trap for charged particles on the second Soviet cosmic rocket. *Sov. Phys. Dokl.* **5**, 361–364 (1960).
3. Neugebauer, M. & Snyder, C. W. Solar plasma experiment. *Science* **138**, 1095–1097 (1962).
4. Somov, B. V. & Syrovatskii, S. I. Appearance of a current (neutral) sheet in a plasma moving in the field of a two-dimensional magnetic dipole. *J. Exp. Theor. Phys.* **34**, 992–997 (1972).
5. Einaudi, G., Chibbaro, S., Dahlburg, R. B. & Velli, M. Plasmoid formation and acceleration in the solar streamer belt. *Astrophys. J.* **547**, 1167–1177 (2001).
6. Fox, N. J. et al. The solar probe plus mission: humanity's first visit to our star. *Space Sci. Rev.* **204**, 7–48 (2016).
7. Szabo, A. Flying into the sun. *Nat. Astron.* **2**, 829–829 (2018).
8. Brooks, D. H., Ugarte-Urra, I. & Warren, H. P. Full-sun observations for identifying the source of the slow solar wind. *Nat. Commun.* **6**, 5947 (2015).
9. Crooker, N. U. et al. Multiple heliospheric current sheets and coronal streamer belt dynamics. *J. Geophys. Res.* **98**, 9371–9381 (1993).
10. Einaudi, G., Boncinelli, P., Dahlburg, R. B. & Karpen, J. T. Formation of the slow solar wind in a coronal streamer. *J. Geophys. Res. Space Phys.* **104**, 521–534 (1999).
11. Parker, E. Dynamical theory of the solar wind. *Space Sci. Rev.* **4**, 666–708 (1965).
12. Mullan, D. J. & Smith, C. W. Solar wind statistics at 1 au: Alfven speed and plasma beta. *Sol. Phys.* **234**, 325–338 (2006).
13. Balogh, A. et al. The heliospheric magnetic field over the south polar region of the Sun. *Science* **268**, 1007–1010 (1995).
14. DeForest, C. E., Howard, R. A., Velli, M., Viall, N. & Vourlidas, A. The highly structured outer solar corona. *Astrophys. J.* **862**, 18 (2018).
15. Cranmer, S. R., Gibson, S. E. & Riley, P. Origins of the ambient solar wind: implications for space weather. *Space Sci. Rev.* **212**, 1345–1384 (2017).
16. Goldstein, B. E. et al. Ulysses plasma parameters: latitudinal, radial and temporal variations. *Astron. Astrophys.* **316**, 296–303 (1996).

17. Antiochos, S. K., Mikić, Z., Titov, V. S., Lionello, R. & Linker, J. A. A model for the sources of the slow solar wind. *Astrophys. J.* **731**, 112 (2011).
18. Sheeley, N. R. Jr. et al. Measurements of flow speeds in the corona between 2 and 30$R_\odot$. *Astrophys. J.* **484**, 472–478 (1997).
19. Wang, Y.-M. et al. Origin of streamer material in the outer corona. *Astrophys. J.* **498**, L165–L168 (1998).
20. Higginson, A. K. & Lynch, B. J. Structured slow solar wind variability: streamer-blob flux ropes and torsional Alfvén waves. *Astrophys. J.* **859**, 6 (2018).
21. Sovinec, C. & King, J. Analysis of a mixed semi-implicit/implicit algorithm for low-frequency two-fluid plasma modeling. *J. Comput. Phys.* **229**, 5803–5819 (2010).
22. Forest, C. B. et al. The Wisconsin plasma astrophysics laboratory. *J. Plasma Phys.* **81**, 345810501 (2015).
23. Levitt, B., Maslovsky, D. & Mauel, M. E. Observation of centrifugally driven interchange instabilities in a plasma confined by a magnetic dipole. *Phys. Rev. Lett.* **94**, 175002 (2005).
24. Birkeland, K. De ľorigine des mondes. *Arch. Sci. Phys. Nat. T.* **35**, 529–564 (1913).
25. Collins, C. et al. Stirring unmagnetized plasma. *Phys. Rev. Lett.* **108**, 115001 (2012).
26. Weisberg, D. B. et al. Driving large magnetic Reynolds number flow in highly ionized, unmagnetized plasmas. *Phys. Plasmas* **24**, 056502 (2017).
27. Köhnlein, W. Radial dependence of solar wind parameters in the ecliptic (1.1$R_\odot$–61 au). *Sol. Phys.* **169**, 209–213 (1996).
28. Zhu, P. & Raeder, J. Plasmoid formation in current sheet with finite normal magnetic component. *Phys. Rev. Lett.* **110**, 235005 (2013).
29. Kivelson, M. G. & Southwood, D. J. Dynamical consequences of two modes of centrifugal instability in Jupiter's outer magnetosphere. *J. Geophys. Res. Space Phys.* **110**, A12209 (2005).
30. Shibasaki, K. High-beta disruption in the solar atmosphere. *Astrophys. J.* **557**, 326–331 (2001).
31. Hood, A. W. Ballooning instabilities in the solar corona: conditions for stability. *Sol. Phys.* **103**, 329–345 (1986).
32. Burch, J. L., Moore, T. E., Torbert, R. B. & Giles, B. L. Magnetospheric multiscale overview and science objectives. *Space Sci. Rev.* **199**, 5–21 (2016).
33. Endeve, E., Holzer, T. E. & Leer, E. Helmet streamers gone unstable: two-fluid magnetohydrodynamic models of the solar corona. *Astrophys. J.* **603**, 307–321 (2004).

Acknowledgements

Author contributions

E.E.P. designed and built the linear Hall probe array, mach and triple probes, executed the experiments and data acquisition, performed all the data analysis and NIMROD simulations and wrote the majority of the text. D.A.E. constructed the magnet, electrode system and capacitor bank trigger circuit and was a partner in running the experiments. D.A.E., M.C., R.W. and E.E.P. constructed the capacitor banks. J.W. designed and constructed motorized probe stages and maintained the vacuum system. C.R.S., K.J.B. and M.B. were instrumental in making modifications to the NIMROD code to be applicable to this experiment and aided in interpreting the simulation results. K.F. and K.J.M. contributed to the compiling of NIMROD. J.M., K.F., J.O. and D.A.E. contributed to construction of the control software and interpreting the data. C.B.F. and J.E. contributed to the interpretation of data and simulations as well as to the writing and editing of the manuscript. C.B.F. is the principal investigator and director of WiPPL, and provided the overall leadership for this project.

Competing interests

The authors declare no competing interests.

Additional information

Supplementary information is available for this paper at https://doi.org/10.1038/s41567-019-0592-7.

Reprints and permissions information is available at www.nature.com/reprints.

Correspondence and requests for materials should be addressed to E.E.P.

Peer review information: *Nature Physics* thanks R. Paul Drake, Nicola Fox and Kristopher Klein for their contribution to the peer review of this work.

Publisher's note: Springer Nature remains neutral with regard to jurisdictional claims in published maps and institutional affiliations.

Methods

Producing an unmagnetized plasma atmosphere. To produce a steady-state plasma atmosphere in the BRB, we start by puffing a small amount of helium into the 3-m-diameter vacuum vessel using piezoelectric valves. This raises the pressure in the vessel from 7×10^{-7} torr to $\sim 5 \times 10^{-5}$ torr, at which point we apply a voltage between -200 V and -400 V to five LaB_6 thermionic cathodes with respect to many grounded anodes. This ionizes the helium and produces a plasma. The multi-dipole confinement scheme of the BRB provides good confinement for this plasma, allowing it to reach an electron temperature of 6.5 eV, density of 4×10^{17} m^{-3} and an ionization fraction of $\sim 25\%$ with an input power of 100 kW for 1.5 s (Fig. 2a,b). This plasma then diffuses into the dipole magnetic field of the SmCo magnet that is placed at the centre of the BRB, providing the base plasma for driving a rotating magnetosphere immersed in an ambient plasma atmosphere.

Driving a rotating magnetosphere. To force rotation, we drive cross-field currents into the magnetosphere, exerting a torque on the plasma. The SmCo magnet has two 3-inch-thin disk molybdenum electrodes fitted near its poles and attached to conductors that carry the current they draw out along the axis of symmetry of the machine. Only a small portion of the outer rim of each electrode is exposed to plasma, creating a virtual cathode flux tube along the field lines that connect the electrodes, as shown in Fig. 1a. During the steady-state portion of the discharge, we apply a -1 kV bias to each electrode with a 56 mF capacitor bank and 1.8 Ω resistor producing a decaying current profile with a peak of ~ 500 A and $\tau = RC = 100$ ms (Fig. 2c). The current going into the magnetosphere comes from grounded anodes in the plasma atmosphere and therefore must cross many field lines to get to the polar electrodes and be extracted. These cross-field currents yield a $J \times B$ torque on the plasma, causing it to rotate.

Data acquisition. Most of the data presented in this Article were produced by linear probe arrays mounted on 2D motorized stages. These stages allowed for scanning in a poloidal plane to build up maps of the 2D time dynamics in the magnetosphere at a given toroidal angle. One scan was performed with a 15-position three-axis Hall sensor array (to measure the magnetic field and currents) and two were performed with a four-position 2D mach and triple probe for measurements of V_φ, V_R, n_e and T_e. During each of these scans, a fixed position reference array of magnetic probes was used to provide phase reference measurements. The resolution of the magnetic maps is ~ 3 cm and for the flow maps is ~ 4 cm. The Hall sensing integrated circuits used (part no. MLX91205KDC-AAL) have a bandwidth of 100 kHz, and were used in a differential output configuration. The signal from each chip was sent directly via twisted pair to differential input digitizers (D-TACQ Solutions ACQ-196). These digitizers sampled the magnetic signals at 200 kHz and directly uploaded raw voltage signals to MDSplus after each shot. The triple probe and mach probe signals were isolated and filtered before digitization by unity gain isolation amplifiers and third-order Bessel filters with a 3 dB point at 100 kHz. Each mach probe face was biased at -120 V with respect to the machine wall (ground). This ensured that the mach probe faces always collected ion saturation current. The 2D maps were built up in a matter of hours, by taking 2–3 shots at each location at a 3 min repetition rate to allow for the capacitor banks to charge and the molybdenum electrodes to cool down.

Data analysis. All of the data taken at the BRB are stored in a hierarchical data tree structure by a software used frequently in the nuclear fusion community called MDSplus. MDSplus trees store probe positions, raw signals, calibration information and error calculations on a shot by shot basis, allowing for much of the signal processing chain to be stored in these trees using relational references and automated scripts. This means that to build the 2D maps shown in Figs. 3 and 4, all that is required is a database of shots for a particular map and the desired time average interval. With this information, all the probe locations and associated signals can be pulled from the trees, averaged over a given period (500 µs in this analysis) and plotted. To calculate absolute velocity measurements, mach probe theory is used to compute the sonic mach number from the ratio of ion saturation current measured by pairs of oppositely facing electrodes. The plasma sound speed is calculated from measurements of the electron temperature by triple probes under the assumptions of cold ions and $Z_{eff} = 1$; these assumptions are justifiable in helium plasmas with these parameters and 100 kW of input power. The sound speed multiplied by the sonic mach number gives the results presented in Fig. 4a. To compute the local Alfvén speed, the magnetic field data are interpolated onto the coarser-resolution density measurements. This is then used to normalize the flow speed to obtain measurements of the Alfvén mach number.

To produce the plasmoid videos, we considered the time period of the shot with the highest correlation across all shots, which turned out to be $\sim t = 1.125$ s. In this time window, the dominant frequency is 20 kHz. Performing a form of conditional averaging based on the mean and fluctuating levels of the stationary reference probe, windows of 500 µs are aligned in time on a shot to shot basis to build up a 2D map of the magnetic field dynamics. The same technique is used with ion saturation current probes to show the phase relationship between density and magnetic field. What this reveals is that magnetic reconnection produces plasmoids that contain higher density than the surrounding plasma, as shown in Supplementary Video 2. Plasmoid velocities were computed from the videos by tracking the 'O'-point of the magnetic islands as they travel outwards.

NIMROD simulations. NIMROD is an extended-MHD code that uses 2D finite element calculations and a Fourier series decomposition in the direction of symmetry to solve the MHD equations. The simulations discussed in this Article were axisymmetric and were performed on a grid of quadrilateral elements resembling a 1.5-m-radius sphere with a 5-cm-radius cylinder removed around $R = 0$ to allow space for the dipole magnet at the centre of the BRB (resembling a cored apple). Both the MHD simulation and Hall-MHD simulation were performed with experimentally similar parameters of $n_e = 4 \times 10^{17}$ m^{-3}, $T_e = 7$ eV and $T_i \approx 0.5$ eV, which gives viscous and resistive diffusivities of $\nu \approx 50$ m^2 s^{-1} and $\eta \approx 30$ m^2 s^{-1}. The effects of neutral particles are included in these simulations through a momentum sink term due to charge exchange with ions. This acts as a drag on the flow, reducing peak flow speeds. No other ionization sources or sinks are modelled in these simulations, but are indeed present in the experiment. The most important difference is the effect of ionization on the virtual cathode flux tube, which would act to enhance the density in the magnetosphere and increase the pressure gradient drive for the plasmoid ejection. The only difference between the two simulations is the addition of the Hall and electron pressure gradient terms in Ohm's law. Each simulation advanced the MHD equations starting from a uniform density and temperature plasma with a dipole magnetic field and a small vertical field to model the axisymmetric (with respect to the machine symmetry) component of Earth's field. During the advance, the current injection used to spin the plasma is prescribed by specifying B_φ on the boundary of the simulation. In all cases the current injection ramps up to a steady-state value in 1 ms and is held constant for the remainder of the simulation.

Data availability

Raw data were generated at the Big Red Ball facility at the Wisconsin Plasma Physics Laboratory. Derived data supporting the findings of this study are available from the corresponding author upon reasonable request.

Code availability

Information about the NIMROD code, including publications and licensing policies, is available at https://nimrodteam.org. Code produced for analysing data at the Big Red Ball Facility is available from the corresponding author upon reasonable request.